

Isotope engineering of van der Waals interactions in hexagonal boron nitride

T. Q. P. Vuong¹, S. Liu², A. Van der Lee³, R. Cuscó⁴, L. Artús⁴, T. Michel¹, P. Valvin¹, J. H. Edgar², G. Cassabois^{1*} and B. Gil¹

Hexagonal boron nitride is a model lamellar compound where weak, non-local van der Waals interactions ensure the vertical stacking of two-dimensional honeycomb lattices made of strongly bound boron and nitrogen atoms. We study the isotope engineering of lamellar compounds by synthesizing hexagonal boron nitride crystals with nearly pure boron isotopes (¹⁰B and ¹¹B) compared to those with the natural distribution of boron (20 at% ¹⁰B and 80 at% ¹¹B). On the one hand, as with standard semiconductors, both the phonon energy and electronic bandgap varied with the boron isotope mass, the latter due to the quantum effect of zero-point renormalization. On the other hand, temperature-dependent experiments focusing on the shear and breathing motions of adjacent layers revealed the specificity of isotope engineering in a layered material, with a modification of the van der Waals interactions upon isotope purification. The electron density distribution is more diffuse between adjacent layers in ¹⁰BN than in ¹¹BN crystals. Our results open perspectives in understanding and controlling van der Waals bonding in layered materials.

Isotopes of a given element have the same number of electrons, but their atomic mass and nuclear spin differ through the number of neutrons. The trivial and prominent effect on isotope exchange is the energy shift of the vibrational excitations. Still, it was realized early that isotopically substituted molecules may react at different rates, a phenomenon known as the kinetic isotope effect^{1,2}, showing that the electronic properties also depend on isotope composition³. In solid state physics, a famous example is the discovery of the isotope effect on the critical temperature of superconductors⁴, which led to the realization of the role of phonons in the formation of Cooper pairs and the development of the Bardeen–Cooper–Schrieffer (BCS) theory of conventional superconductors. The extension of isotopic purification to semiconductors has further triggered a wealth of fundamental studies in this class of crystals⁵. More recently, in the context of quantum computation and sensing, the use of isotope engineering has appeared as an important resource for preserving the quantum information, or encoding a qubit on a nuclear spin^{6–8}.

Interest in layered compounds is increasing because of their unique properties at the monolayer level, and the possibility of assembling them into van der Waals heterostructures⁹. Graphite, transition metal dichalcogenides, and hexagonal boron nitride (hBN) are generic examples, displaying the typical strong in-plane binding contrasting with the weak interlayer coupling due to van der Waals interactions. As such, they present some similarities with hydrogen-bonded systems, where the intermolecular geometric isotope effect in hydrogen bonds is known in chemistry as the Ubbelohde effect¹⁰. Layered compounds provide a model test bed for investigating the impact of isotopic substitution on van der Waals interactions. We open here the field of isotope engineering of such crystals with the example of hBN.

Besides the investigation of fundamental effects, the fabrication of isotopically purified hBN crystals was also motivated by their

potential applications. For example, the ¹⁰B and ¹¹B isotopes are strong and weak thermal neutron absorbers, respectively, hence ¹⁰B has many applications in nuclear energy industries¹¹ and cancer treatment by boron neutron capture therapy¹². In the case of hBN, the room temperature thermal conductivity is predicted to increase by 40% with isotopically pure boron of either type¹³. Isotopically pure hBN also has polariton lifetimes an order of magnitude higher than hBN with the natural distribution of boron, due to reduced phonon scattering¹⁴.

Isotopic ¹⁰B- and ¹¹B-enriched hBN crystals were precipitated from a molten metal flux of nickel and chromium using the process described by Hoffman *et al.*¹⁵ modified by using high-purity elemental boron-10 (¹⁰B at 99.2%) and boron-11 (¹¹B at 99.4%) powders instead of hBN powder as the source, nitrogen-14 having a natural abundance of 99.6% (Supplementary Section A). We combined Raman scattering, photoluminescence, and X-ray diffraction for the characterization of our isotopically purified hBN crystals (Supplementary Section A), which are systematically compared to a standard sample ^{nat}BN (schematically depicted in Fig. 1a) displaying the natural abundance at 20–80% of ¹⁰B and ¹¹B, respectively.

Phonon energy

The frequency of lattice vibrations decreases with the atomic mass; this universal behaviour is inherited from the frequency ($\sqrt{k/m}$) of the harmonic oscillator. Therefore, when varying the isotope, the frequency of phonons varies. This effect is the simplest consequence of isotope substitution, which can be monitored by Raman scattering. hBN is a lamellar crystal that crystallizes in the $P6_3/mmc$ space group and contains four atoms in the unit cell. The zone-centre optical phonons belong to the $E_{1u} + A_{2u} + 2E_{2g} + 2B_{1g}$ irreducible representations of the D_{6h} point group. The E_{1u} and A_{2u} modes are infrared active while the B_{1g} are silent modes. Only the E_{2g} modes, which involve in-plane atomic displacements in the

¹Laboratoire Charles Coulomb (L2C), Université de Montpellier, CNRS, 34095 Montpellier, France. ²Department of Chemical Engineering, Kansas State University, Manhattan, Kansas 66506, USA. ³Institut Européen des Membranes, UMR 5635 CNRS-Univ. Montpellier-ENSCM, 34095 Montpellier, France.

⁴Institut Jaume Almera, Consejo Superior de Investigaciones Científicas (ICTJA-CSIC), 08028 Barcelona, Spain.

*e-mail: guillaume.cassabois@umontpellier.fr

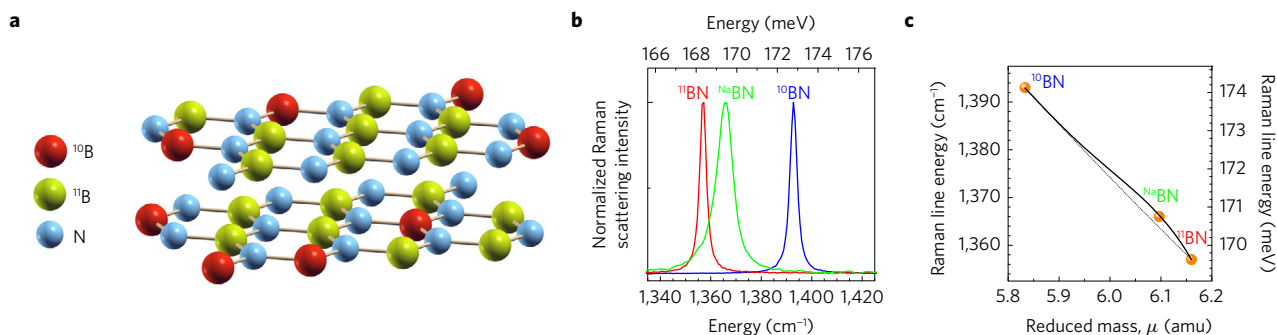


Figure 1 | Isotope mass dependence of vibrational excitations. **a**, Honeycomb lattice in natural hexagonal boron nitride (^{Na}BN) showing the isotopic mixture of boron-10 (red) and boron-11 (green) atoms bound to nitrogen-14 (blue). **b**, Raman scattering spectra in ^{10}BN , ^{Na}BN and ^{11}BN , at room temperature. **c**, Raman mode energy versus reduced mass μ in hBN: $\mu^{-1/2}$ mass dependence in the virtual crystal approximation (dashed line), energy shift due to isotopic mass disorder $+\mu^{-1/2}$ mass dependence (solid line).

hexagonal layers, are Raman active. Figure 1b displays the Raman scattering spectrum in ^{10}BN , ^{Na}BN and ^{11}BN around $1,400\text{ cm}^{-1}$ (170 meV). The Raman line in Fig. 1b corresponds to the high-energy E_{2g} mode, in which boron and nitrogen atoms vibrate against each other in the hexagonal layer¹⁶. The energy of this E_{2g}^{high} phonon is $1,393\text{ cm}^{-1}$ ($1,357\text{ cm}^{-1}$) for ^{10}BN (^{11}BN , respectively), with an intermediate value of $1,366\text{ cm}^{-1}$ for the isotopic mixture in ^{Na}BN . In addition to the decrease of the phonon energy with the mass of the boron isotope, the linewidth is also lower in the isotopically pure crystals ^{10}BN and ^{11}BN (Fig. 1b). In ^{10}BN and ^{11}BN , the full-width at half-maximum of the Raman line is 3 cm^{-1} compared to 7.5 cm^{-1} in ^{Na}BN .

The broadening of the Raman line in ^{Na}BN originates from static isotopic mass disorder that breaks the translational invariance and induces elastic scattering of phonons⁵. This disorder-induced broadening is the imaginary part of the self-energy due to the isotopic mass fluctuations, the real part being an energy shift of the same order of magnitude as the imaginary part¹⁷. In Fig. 1c, displaying the energy of the Raman-active optical phonon as a function of the reduced mass μ in hBN, we obtain an excellent agreement (solid line) with our experimental data by taking into account the energy shift due to static isotopic mass disorder (see Supplementary Section C for more details on static mass disorder) in addition to the trivial mass dependence as $\mu^{-1/2}$ (dashed line) in the virtual crystal approximation^{5,18}. The energy shift used for the fit (solid line, Fig. 1c) accounts for the maximum displacement of 2.5 cm^{-1} (0.3 meV)—that is, a value comparable to the Raman line-broadening (Fig. 1b), consistent with the phenomenology in other compounds¹⁷.

Electronic bandgap

Besides the vibrational excitations, the isotope mass also impacts the electronic properties because of the electron–phonon interaction. A well-known effect concerns the zero-point renormalization of the bandgap⁵. The electronic states are renormalized to second order in the phonon amplitude u because of the so-called Fan and Debye–Waller terms in second-order perturbation theory, but also because of anharmonic terms responsible for thermal expansion in the first-order perturbation. At zero temperature, the bandgap energy eventually depends on the zero-point vibrations ($\langle u^2 \rangle$), the average value being calculated over all phonon modes. The renormalization of the bandgap at zero temperature is thus a true quantum effect related to the zero-point vibrations. Since the renormalization energy δE_g scales as $\mu^{-1/2}$, isotopic substitution changes the bandgap of a semiconductor at low temperature, as demonstrated for instance in silicon, germanium and diamond⁵.

This phenomenon was investigated in our isotopically engineered hBN crystals by photoluminescence (PL) spectroscopy. In this wide bandgap semiconductor^{19–21}, the intrinsic optical response

lies in the deep ultraviolet around 6 eV (200 nm), as seen in Fig. 2a, displaying the PL spectra in ^{10}BN , ^{Na}BN and ^{11}BN at 8 K . Because hBN is an indirect bandgap semiconductor^{22–25}, phonon emission is required for momentum conservation with luminescence. As a matter of fact, the PL spectrum is composed of many emission lines, reflecting the various paths for recombination assisted by phonon emission. The larger the phonon energy, the larger the energy detuning with the indirect bandgap at around 5.95 eV (ref. 22), and thus the lower the energy of the phonon replica. In Fig. 2a, the four peaks at 5.76 , 5.79 , 5.86 and 5.89 eV correspond to recombination assisted by the emission of phonons of decreasing energy, more specifically one LO, TO, LA and TA phonon, respectively^{22–25}.

Upon isotope purification, the PL spectrum is globally blue-shifted in ^{11}BN compared to ^{Na}BN , while it is red-shifted in ^{10}BN (Fig. 2a). Moreover, the lower the energy of the phonon replicas, the higher the splitting between the PL lines of ^{10}BN , ^{Na}BN and ^{11}BN . The latter effect is the counter-part, in the phonon-assisted PL spectrum of hBN, of the isotope mass dependence of the lattice vibrations discussed above. Since the absolute isotopic shift of a phonon mode increases with its energy, the splitting of the phonon replicas is more pronounced for the emission lines lying at lower energy.

To separate the isotopic shift of the phonon modes from the isotope-dependent renormalization of the bandgap energy δE_g , we have plotted in Fig. 2b the energy of the emission lines at 8 K as a function of the phonon energy (the weak ZA phonon replica at 5.93 eV being observable only on a log scale^{22,23}). We stress that the complete phonon bandstructure was calculated for each isotopic composition to obtain accurate values of the vibrational excitations in ^{10}BN , ^{Na}BN and ^{11}BN . For each crystal, we obtain a fair agreement of our experimental data with a linear fit $E_i - E_{\text{vib}}$ (solid lines in Fig. 2b), where E_{vib} is the isotope-dependent phonon energy and E_i the indirect bandgap energy, equal to $5,960$, $5,958.5$ and $5,954\text{ meV}$ in ^{11}BN , ^{Na}BN and ^{10}BN , respectively. Besides confirming the isotopic shift of the phonon replicas in hBN, our analysis demonstrates that the bandgap energy depends on the isotope mass.

The variations of the indirect bandgap E_i with the isotopic composition are more clearly resolved in the left inset of Fig. 2b, displaying the energy shift of the phonon replicas in ^{10}BN and ^{11}BN compared to ^{Na}BN , after subtracting the isotopic shift of the corresponding phonon mode. The average over the five types of phonon replicas (dashed lines in Fig. 2b, left inset) provides estimates of 1.6 ± 0.2 and $-4.4 \pm 0.2\text{ meV}$ for the indirect bandgap E_i shift in ^{11}BN and ^{10}BN , respectively, compared to ^{Na}BN . These values are precisely the variations of the bandgap renormalization δE_g with the isotope mass, namely $\delta E_g^{11} - \delta E_g^{Na} = 1.6 \pm 0.2\text{ meV}$ and $\delta E_g^{10} - \delta E_g^{Na} = -4.4 \pm 0.2\text{ meV}$. In the right inset of Fig. 2b, where we display them as a function of the reduced mass, the solid line is a fit as $\mu^{-1/2}$, where the bandgap renormalization in ^{Na}BN is

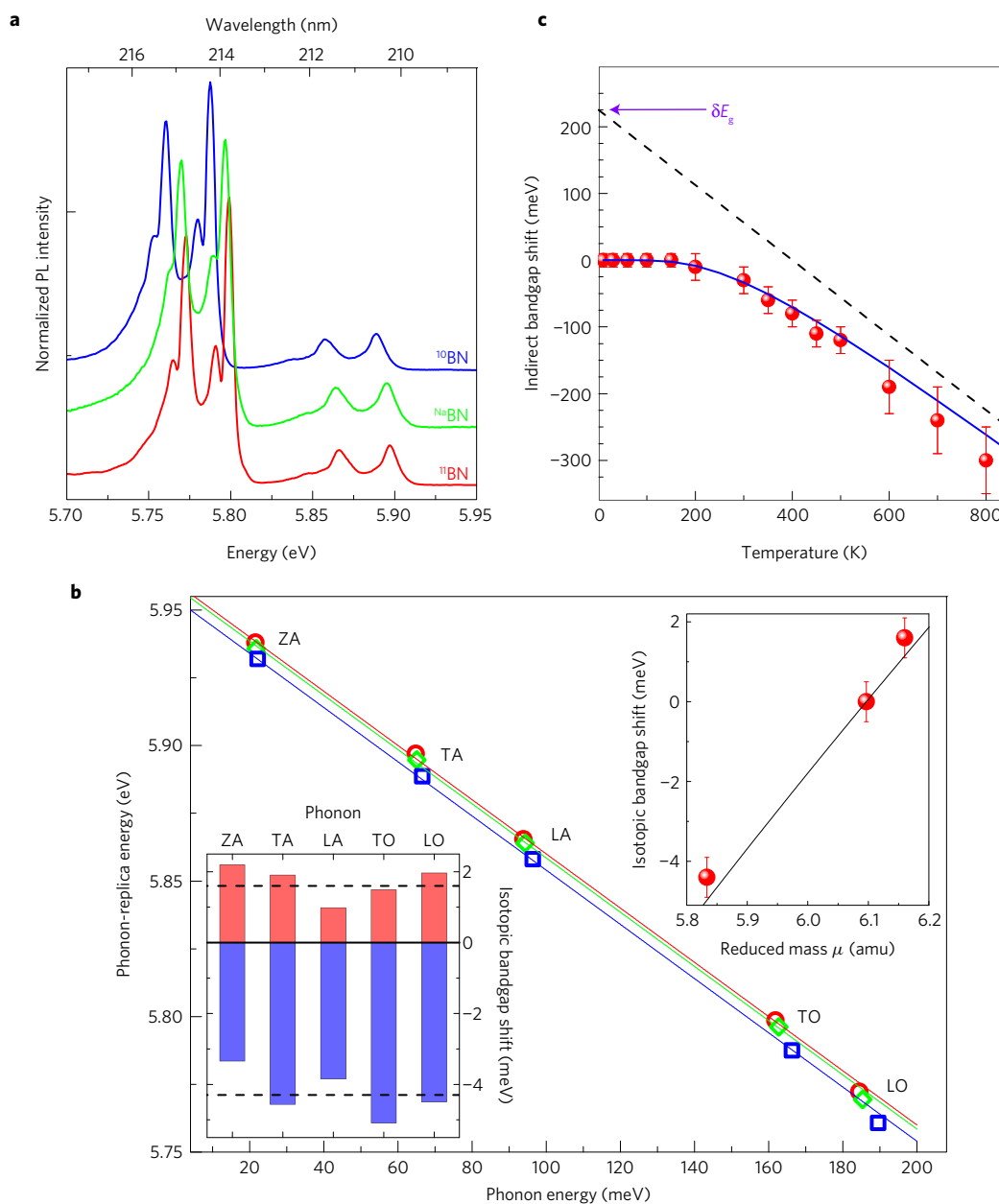


Figure 2 | Isotope mass dependence of the bandgap energy due to zero-point renormalization. a, PL spectrum for ^{10}BN , $^{\text{Na}}\text{BN}$ and ^{11}BN at 8 K. **b**, Energy of phonon replicas versus calculated isotope-dependent phonon energy at 8 K. Left inset: energy shift of the phonon replica in ^{10}BN (blue bars) and ^{11}BN (red bars) compared to $^{\text{Na}}\text{BN}$, after subtraction of the isotopic shift of the phonon modes. Right inset: isotopic dependence of bandgap renormalization δE_g . **c**, Temperature dependence of the indirect bandgap: data from ref. 27 (symbols, where error bars indicate the standard deviations for least-squares fitting of the emission spectrum), single oscillator fit (solid line, see text), and high-temperature asymptotic linear limit of the single oscillator fit with a slope $-2k_B\delta E_g/\Omega$ (dashed line).

the only parameter (Supplementary Section C). We obtain a value $\delta E_g^{\text{Na}} = 225 \pm 10$ meV.

In isostructural cubic semiconductors such as germanium, silicon and diamond, the renormalization energy δE_g increases with the bandgap⁵. Although hBN and diamond are both indirect semiconductors with a similar bandgap of about 6 eV, δE_g is approximately twice as large in diamond^{5,26}, revealing the specificity of the electron–phonon interaction in a lamellar compound such as hBN.

Furthermore, by estimating δE_g in hBN, one gets an instructive insight into the temperature dependence of the bandgap. While the zero-point renormalization energy δE_g involves all phonon modes, there is a phenomenological ansatz approximating the full phonon dispersion with a single Einstein oscillator of energy Ω .

The thermally assisted bandgap shift is then reproduced by using $\Delta E_i(T) = -\delta E_g(1 + 2/[e^{\Omega/k_B T} - 1])$ (refs 5,26). Adjusting the temperature-dependent data recorded up to 800 K in ref. 27 (symbols, Fig. 2c), we obtain $\Omega = 68 \pm 2$ meV. Compared to the absolute maximum of the phonon dispersion of 200 meV in hBN (ref. 16), we obtain a ratio of 0.34, significantly lower than the usual one-half found in cubic semiconductors⁵. Since the Einstein parameter Ω in layered hBN is rather low, this indicates that the interlayer vibrations (which have lower energies than the intralayer ones) make a significant contribution to the electron–phonon bandgap renormalization. Still, one cannot exclude that the acoustic phonons might play a more important role in layered compounds than in the cubic crystals discussed by Cardona and Thewalt⁵. The

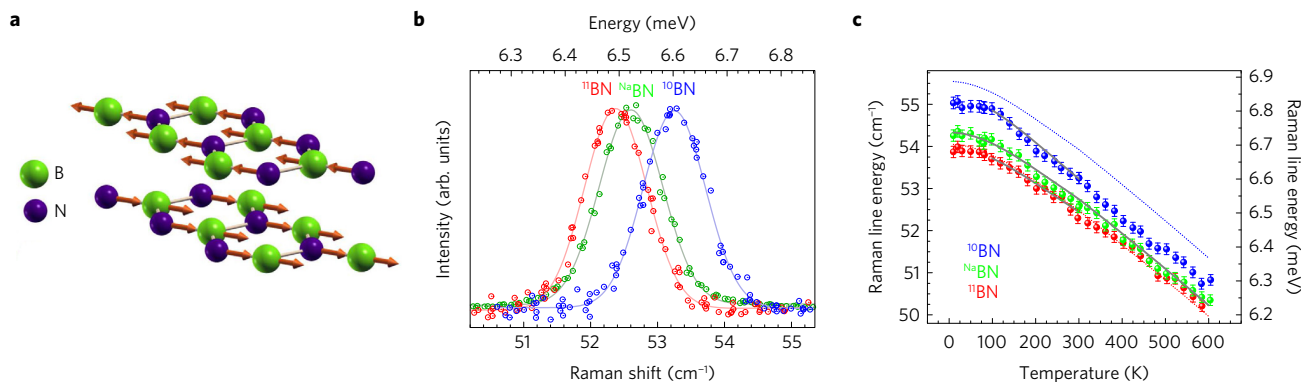


Figure 3 | Shear motion of adjacent layers. **a**, Schematic representation of the atomic motion for the E_{2g}^{low} interlayer shear mode. **b**, High-resolution Raman spectra for the E_{2g}^{low} interlayer shear mode in ^{10}BN , $^{\text{Na}}\text{BN}$ and ^{11}BN at 300K. **c**, Temperature dependence of the frequency shift for the E_{2g}^{low} interlayer shear mode in ^{10}BN , $^{\text{Na}}\text{BN}$ and ^{11}BN : experimental data (symbols, where error bars indicate the standard deviations for least-squares fitting of the Raman spectrum) and fits with a $1/c^p$ power-law dependence of the E_{2g}^{low} interlayer shear mode energy with the c -lattice parameter (solid lines). The dotted lines correspond to a trivial mass scaling as $\mu^{-1/2}$ of the energy of the interlayer shear mode in $^{\text{Na}}\text{BN}$.

elucidation of this novel phenomenology will require microscopic calculations of the Einstein parameter Ω in the framework of the theoretical approaches developed in refs 28–30.

The first part of this paper addressed text-book aspects of isotopic concentration on the properties of semiconductors⁵. The quantitative interpretation of the phonon energy and electronic bandgap in ^{10}BN , $^{\text{Na}}\text{BN}$ and ^{11}BN indicates the excellent quality of our crystals. In the second part of this paper, we focus on previously unexplored aspects of isotope engineering. We investigate the impact of isotope concentration on the peculiar lattice vibrations of van der Waals crystals, corresponding to rigid motions of adjacent layers.

Interlayer shear mode

We first address the E_{2g}^{low} mode, which corresponds to the interlayer shear mode schematically represented in Fig. 3a. Interlayer shear modes yield low-energy vibrational excitations in graphite³¹, molybdenum disulfide³², and hBN¹⁶ because of the weak van der Waals coupling between adjacent layers. As can be seen in Fig. 3b, the E_{2g}^{low} interlayer shear mode of hBN decreases in energy with the mass of the boron isotope, likewise the E_{2g}^{high} mode, and at low temperatures it displays energies around 54.5 cm^{-1} ($\sim 6.7 \text{ meV}$) in the samples with different isotopic composition.

Regarding the temperature dependence of the interlayer shear mode, this is solely attributed to the positive thermal expansion coefficient along the c -axis. This is in contrast with the high-energy Raman-active phonon (Fig. 1b), in which the effects of the negative thermal expansion coefficient in the basal plane are overcompensated by the anharmonic processes¹⁶. Figure 3c shows the energy variations recorded between 10 and 600 K for each hBN crystal. Surprisingly, the thermal red-shift of the interlayer shear mode does depend on the isotopic composition, with the highest (lowest) variations for ^{10}BN (^{11}BN , respectively).

It is instructive to consider the underlying physics by analysing the power-law dependence of the interlayer shear mode energy with the c -lattice parameter. In the case of $^{\text{Na}}\text{BN}$, the thermal expansion along the c -axis was accurately studied between 10 and 600 K (refs 33,34). The thermal red-shift of the interlayer shear mode fairly reproduces these measurements by using a $1/c^p$ law, with $p = 3.6 \pm 0.1$, as shown by the solid line in Fig. 3c. Such variations stem from the square root dependence of the phonon energy with the phonon force constant k . It is itself proportional to the C_{2n} coefficients weighting the $1/r^{2n}$ terms in the series expansion of the van der Waals potential with the interatomic distance, so that one eventually finds $p \sim n + 1$ (Supplementary Section C). In ref. 35, Popov *et al.* used a tight-binding model with matrix elements derived within the density functional theory, to study the interplay

between the repulsive interlayer band energy and the weak attractive van der Waals interactions (this issue was also addressed by other theoretical approaches, such as density functional approximations including non-local many-body dispersion interactions³⁶). In their semi-empirical calculations, Popov *et al.* found that the C_{2n} coefficients with $n = 3$ and 4 are the dominant contributions in graphite. Consequently, one expects a $1/c^p$ dependence of the thermal shift of the interlayer shear mode, with p of about 4 to 5. To the best of our knowledge, this issue has never been addressed in the literature.

We now come back to the isotopic dependence of the $1/c^p$ law, revealed by Fig. 3c. Importantly, we stress that the measurements in ^{10}BN deviate from a trivial mass scaling as $\mu^{-1/2}$ (dotted line in Fig. 3c) of the energy of the interlayer shear mode in $^{\text{Na}}\text{BN}$. On the one hand, temperature-dependent single-crystal diffraction experiments did not show significantly different values, within our experimental error, for the thermal expansion along the c -axis between ^{10}BN , $^{\text{Na}}\text{BN}$ and ^{11}BN (Supplementary Fig. 1, Supplementary Section B). On the other hand, the p -exponent does present a striking dependence on the isotopic composition. The quantitative analysis of our measurements in isotopically purified hBN crystals (Fig. 3c) concludes to a variation of the $1/c^p$ power-law dependence of the interlayer shear mode, with modifications of the p -exponent from one sample to another. While $p = 3.6 \pm 0.3$ in ^{11}BN , it increases to 5.7 ± 0.3 in ^{10}BN , as a result of the larger thermal red-shift observed in Fig. 3c (see Supplementary Section C for more details on the quantitative analysis). This is the first indication that the weak, non-local van der Waals coupling varies with the isotopic composition.

Interlayer breathing mode

The second case of interest is the B_{1g} interlayer breathing mode, schematically represented in Fig. 4a. This phonon corresponds to the anti-phase rigid motion of adjacent layers along the c -axis. It has a higher energy than the E_{2g}^{low} interlayer shear mode, since the latter is related to the C_{44} shear elastic constant whereas the former is related to the C_{33} compression elastic constant, with the natural hierarchy $C_{44} < C_{33}$ in graphitic systems³⁷. Importantly, the B_{1g} interlayer breathing mode is neither Raman nor infrared active by symmetry, so that the direct investigation of this silent mode is not possible by optical spectroscopy³⁸.

However, the B_{1g} interlayer breathing mode contributes to the thermally assisted broadening of the emission spectrum in hBN, as recently demonstrated in ref. 39. Above 70 K, absorption of such phonons is in fact the dominant broadening process so that the study of the temperature-dependent linewidth in PL spectroscopy provides an accurate measure of the exciton–phonon coupling for

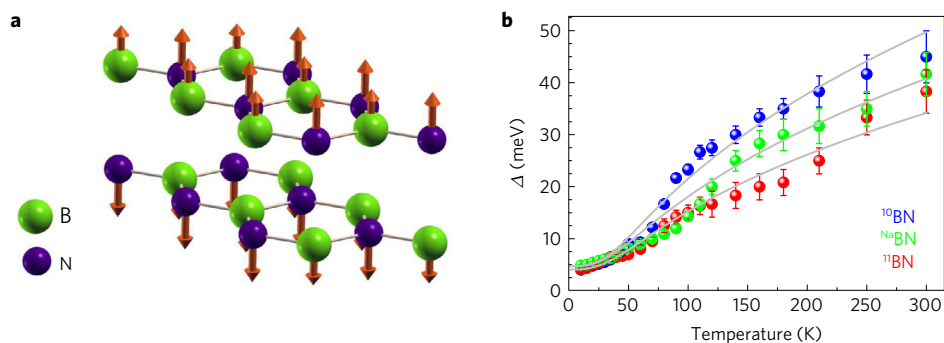


Figure 4 | Breathing motion of adjacent layers. **a**, Schematic representation of the atomic motion for the B_{1g} interlayer breathing mode. **b**, Phonon-assisted broadening Δ of the PL spectra in ^{10}BN , ^{15}BN and ^{11}BN : experimental data (symbols), fits of the thermally induced broadening (solid lines). Error bars indicate the standard deviations of Δ for least-squares fitting of the emission spectrum within the framework detailed in ref. 39.

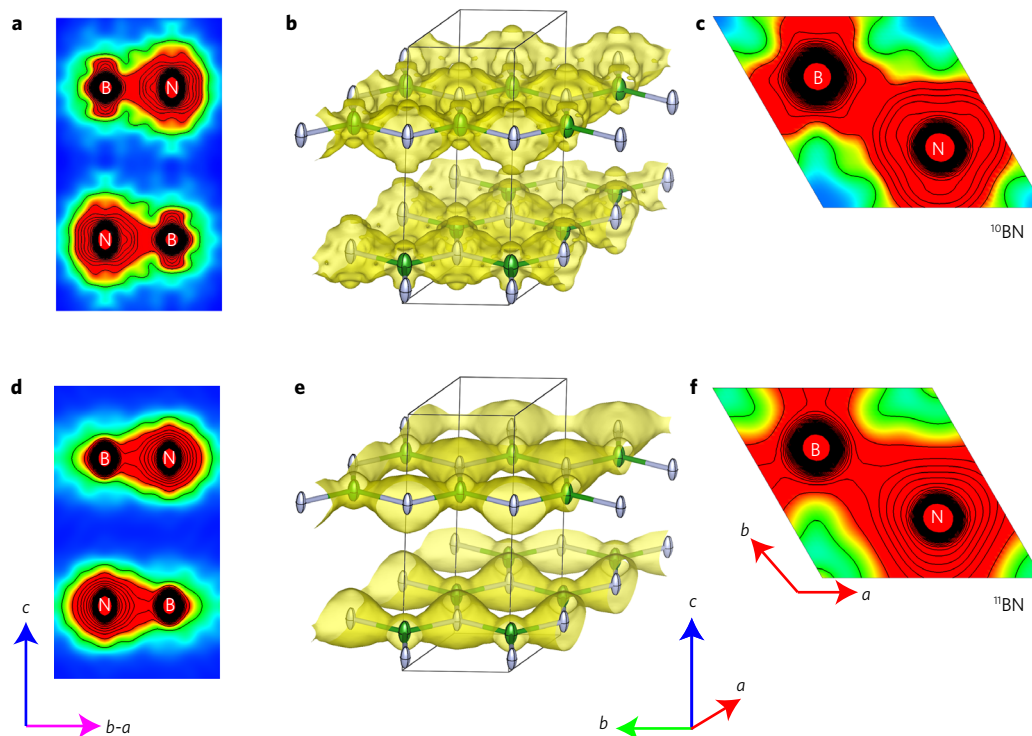


Figure 5 | Electronic density in ^{10}BN and ^{11}BN . Electron density distribution in ^{10}BN (**a–c**) and ^{11}BN (**d–f**) using the maximum entropy method against X-ray data collected at 125 K to 0.4 Å resolution. **a,d**, 2D contour plots in a plane parallel to the c -axis. **b,e**, Side view of 3D contour plots with an iso-contour level at $1 \text{ e} \text{ \AA}^{-3}$. **c,f**, 2D contour plots in a plane perpendicular to the c -axis. The iso-contour levels range from 1 to $30 \text{ e} \text{ \AA}^{-3}$ in steps of $0.5 \text{ e} \text{ \AA}^{-3}$.

this specific type of lattice vibrations. Figure 4b shows the PL line-broadening Δ as a function of temperature for ^{10}BN , ^{15}BN and ^{11}BN . The strength of the model employed for extracting the linewidth is the use of a single fitting parameter Δ for reproducing the full PL spectrum of bulk hBN in the deep ultraviolet. As detailed in ref. 39, once the low-temperature PL spectrum is accurately reproduced with the different, calculated values of the phonon group velocities, the temperature-dependent PL spectrum is adjusted by varying only Δ , which is identical for all phonon replicas. This robust fitting procedure allows us to fairly account for the complete set of measurements. As for the case of the interlayer shear mode (Fig. 3), again there is a striking dependence of the thermal broadening on the isotopic composition, with the highest (lowest) phonon-assisted broadening for ^{10}BN (^{11}BN , respectively).

The solid lines in Fig. 4b are fits of the thermally induced broadening according to the expression $\Delta = \sqrt{\Delta_A^2 + \Delta_O^2}$, where Δ_A and Δ_O are the broadenings due to the low-energy acoustic phonons and the B_{1g} interlayer breathing mode, respectively³⁹. Δ_A is the

dominant broadening term below 70 K, and it is insensitive to the isotopic composition within our experimental error. In contrast, above 70 K, where Δ_O prevails, the coupling strength S_0 to the B_{1g} interlayer breathing mode (Supplementary Section C) increases from 50 ± 10 , to 70 ± 10 , and then $115 \pm 10 \text{ meV}$ in ^{11}BN , ^{15}BN and ^{10}BN , respectively. Such variations cannot be accounted for by considerations either on the isotopic energy shift of this phonon, or on the deformation potential coupling excitons to the B_{1g} interlayer breathing mode (see Supplementary Section C for more details). Similar to the case of the shear motion of adjacent layers, we infer that isotope engineering in hBN impacts the lattice vibrations controlled by the weak van der Waals coupling between adjacent layers.

Electron density distribution

In the last part of our paper, we demonstrate that the interlayer electronic distribution itself is affected by the isotopic substitution. This striking phenomenon is revealed by X-ray diffraction experiments. Electron density maps were determined using the

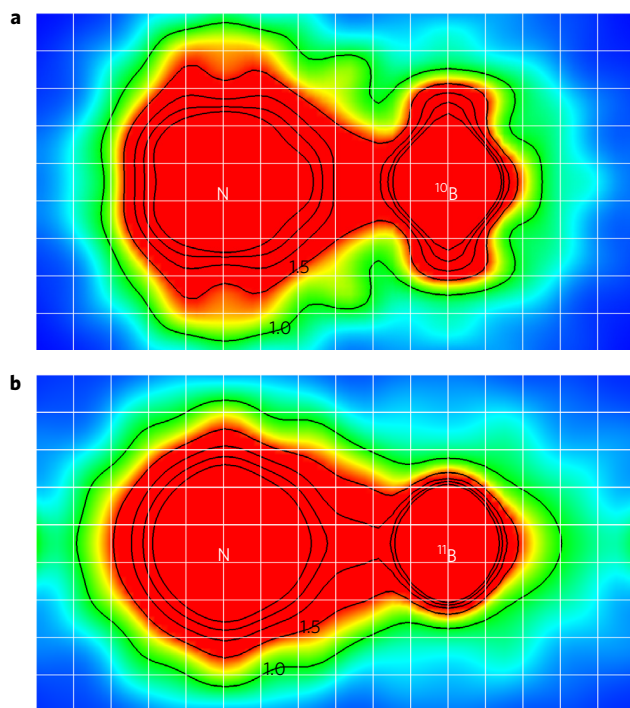


Figure 6 | Electronic isodensity contours in a plane parallel to the c-axis. **a,b**, Expanded view of Fig. 5a,d for ^{10}BN (**a**) and ^{11}BN (**b**). The orientation is identical to Fig. 5a,d, but the vertical section is between $z = 0.585$ and $z = 0.915$ in crystallographic units of the c -lattice parameter ($c \sim 6.6 \text{ \AA}$). Contour levels are from 1 to 3 e \AA^{-3} in steps of 0.5 e \AA^{-3} . Squares in the white grids have a size of 0.242 \AA .

maximum entropy method (MEM)⁴⁰ against X-ray data collected at 125 K to 0.4 \AA resolution (Fig. 5). The three-dimensional (3D) isosurface and two-dimensional (2D) contour plots show the electron density around N protruding towards ^{10}B and ^{11}B , in accordance with experimental electron density maps determined from powder data on natural hBN⁴¹, and also with *ab initio* calculations^{42,43}. Importantly, the gridded and expanded maps in Fig. 6 show that the out-of-plane electron density is more spread out (inwards the van der Waals gap) around both nuclei in ^{10}BN than in ^{11}BN . This is also quantitatively demonstrated by the larger apparent atomic displacement parameters resulting from structural refinements using high-resolution data between 0.8 and 0.4 \AA (see Supplementary Table 2 in Supplementary Section B), which are less sensitive to contributions of delocalized and/or valence electrons. One paper reported a different electron density distribution in 3D covalently bound crystals such as ^{12}C and ^{13}C diamond⁴⁴. Our study reveals the isotopic modification of the electronic density in-between layers coupled by the van der Waals interaction.

The different neutron numbers of isotopes are expected to induce slight modifications in the electronic wavefunction. Because of the finite nucleus size, the Coulomb potential experienced by electrons deviates from the case of point-like nuclei, resulting in the so-called field shift, which increases with nuclear size⁴⁵. The hyperfine effect due to the deformation of the nuclear charge distribution is, however, in the gigahertz range⁴⁵, that is, three orders of magnitude lower than the characteristic spectral shifts discussed here. Similarly, the coupling to the nuclear spin (^{10}B and ^{11}B having a spin of 3 and 3/2, respectively) is another hyperfine phenomenon, leading to the Overhauser shift, but upon optical pumping so that we can also rule out this possibility in our X-ray diffraction experiments.

The most plausible interpretation for the deformation of the electron wavefunctions in-between the layers of isotopically purified hBN crystals goes back to the mass variations in ^{10}B and ^{11}B nuclei.

Our phenomenology resembles the one described in the context of isotopic substitution in BrLBr isotopomers, where L is an isotope of hydrogen⁴⁶. By quantum chemistry calculations, a fundamental change of the chemical bonding was established from van der Waals bonding to the so-called vibrational bonding when decreasing the mass of the hydrogen isotope⁴⁶. Even if our whole set of measurements (Figs 3–6) demonstrate an isotopic tuning of van der Waals interactions in a model layered compound, we are probably far from vibrational bonding in ^{10}BN . Moreover, one should also consider the coupling of low-energy vibrational modes to collective electron density fluctuations in our layered compound. As recently demonstrated in a different system, non-local many-body van der Waals interactions can lead to a renormalization of the phonon density of states^{47,48}, which may be significant and isotope-dependent in hBN.

Our results pave the way for future experiments in isotopically engineered layered compounds (graphite being one evident candidate), isotopic heterostructures⁴⁹, or isotopic superlattices for magnetic resonance spectroscopy⁵⁰. Because it is difficult to calculate weak van der Waals interactions compared to intralayer covalent bonds, our study should also stimulate future developments in *ab initio* calculations to properly account for the isotope tuning of the non-local interactions determining the cohesion of layered compounds.

Methods

Methods, including statements of data availability and any associated accession codes and references, are available in the [online version of this paper](#).

Received 17 May 2017; accepted 1 November 2017;
published online 11 December 2017

References

- Bigeleisen, J. & Goeppert-Mayer, M. Calculation of equilibrium constants for isotopic exchange reactions. *J. Chem. Phys.* **15**, 261–267 (1947).
- Simmons, E. M. & Hartwig, J. F. On the interpretation of deuterium kinetic isotope effects in C-H bond functionalizations by transition-metal complexes. *Angew. Chem. Int. Ed.* **51**, 3066–3072 (2012).
- Kohen, A. & Limbach, H.-H. *Isotope Effects in Chemistry and Biology* (CRC Press, 2006).
- Maxwell, E. Isotope effect in the superconductivity of mercury. *Phys. Rev.* **78**, 477 (1950).
- Cardona, M. & Thewalt, M. L. W. Isotope effects on the optical spectra of semiconductors. *Rev. Mod. Phys.* **77**, 1173–1224 (2005).
- Kane, B. E. A silicon-based nuclear spin quantum computer. *Nature* **393**, 133–137 (1998).
- Balasubramanian, G. *et al.* Ultralong spin coherence time in isotopically engineered diamond. *Nat. Mater.* **8**, 383–387 (2009).
- Itoh, K. M. & Watanabe, H. Isotope engineering of silicon and diamond for quantum computing and sensing applications. *MRS Commun.* **4**, 143–157 (2014).
- Geim, A. K. & Grigorieva, I. V. Van der Waals heterostructures. *Nature* **499**, 419–425 (2013).
- Ikabata, Y., Imamura, Y. & Nakai, H. Interpretation of intermolecular geometric isotope effect in hydrogen bonds: nuclear orbital plus molecular orbital study. *J. Phys. Chem. A* **115**, 1433–1439 (2011).
- Subramanian, C., Suri, A. K. & Ch. Murthy, T. S. R. Development of boron-based materials for nuclear applications. *BARC Newsletter* **313**, 14–22 (2010).
- Barth, R. F., Soloway, A. H., Fairchild, R. G. & Brugger, R. M. Boron neutron capture therapy for cancer. Realities and prospects. *Cancer* **70**, 2995–3007 (1992).
- Lindsay, L. & Broido, D. A. Enhanced thermal conductivity and isotope effect in single-layer hexagonal boron nitride. *Phys. Rev. B* **84**, 155421 (2011).
- Giles, A. J. *et al.* *Nat. Mater.* <http://dx.doi.org/10.1038/nmat5047> (2017).
- Hoffman, T. B., Clubine, B., Zhang, Y., Snow, K. & Edgar, J. H. Optimization of NiCr flux growth for hexagonal boron nitride single crystals. *J. Crystal Growth* **393**, 114–118 (2014).
- Cuscó, R., Gil, B., Cassabois, G. & Artús, L. Temperature dependence of Raman-active phonons and anharmonic interactions in layered hexagonal BN. *Phys. Rev. B* **94**, 155435 (2016).

17. Göbel, A., Ruf, T., Zhang, J. M., Lauck, R. & Cardona, M. Phonons and fundamental gap in ZnSe: effects of the isotopic composition. *Phys. Rev. B* **59**, 2749–2759 (1999).
18. Hass, K. C., Tamor, M. A., Anthony, T. R. & Banholzer, W. F. Lattice dynamics and Raman spectra of isotopically mixed diamond. *Phys. Rev. B* **45**, 7171–7182 (1992).
19. Watanabe, K., Taniguchi, T. & Kanda, H. Direct-bandgap properties and evidence for ultraviolet lasing of hexagonal boron nitride single crystal. *Nat. Mater.* **3**, 404–409 (2004).
20. Watanabe, K., Taniguchi, T., Niiyama, T., Miya, K. & Taniguchi, M. Far-ultraviolet plane-emission handheld device based on hexagonal boron nitride. *Nat. Photon.* **3**, 591–594 (2009).
21. Watanabe, K. *et al.* Hexagonal boron nitride as a new ultraviolet luminescent material and its application—Fluorescence properties of hBN single-crystal powder. *Diam. Relat. Mater.* **20**, 849–852 (2011).
22. Cassabois, G., Valvin, P. & Gil, B. Hexagonal boron nitride is an indirect bandgap semiconductor. *Nat. Photon.* **10**, 262–266 (2016).
23. Vuong, T. Q. P. *et al.* Phonon symmetries in hexagonal boron nitride probed by incoherent light emission. *2D Mater.* **4**, 11004 (2017).
24. Vuong, T. Q. P. *et al.* Overtone emission spectrum of hexagonal boron nitride. *Phys. Rev. B* **95**, 45207 (2017).
25. Cassabois, G., Valvin, P. & Gil, B. Intervalley scattering in hexagonal boron nitride. *Phys. Rev. B* **93**, 35207 (2016).
26. Giustino, F., Louie, S. G. & Cohen, M. L. Electron-phonon renormalization of the direct band gap of diamond. *Phys. Rev. Lett.* **105**, 265501 (2010).
27. Du, X. Z., Frye, C. D., Edgar, J. H., Lin, J. Y. & Jiang, H. X. Temperature dependence of the energy bandgap of two-dimensional hexagonal boron nitride probed by excitonic photoluminescence. *J. Appl. Phys.* **115**, 53503 (2014).
28. Allen, P. B. & Heine, V. Theory of the temperature dependence of electronic band structures. *J. Phys. C* **9**, 2305–2312 (1976).
29. Lautenschlager, P., Garriga, M. & Cardona, M. Temperature dependence of the interband critical-point parameters of InP. *Phys. Rev. B* **36**, 4813–4820 (1987).
30. Zollner, S., Cardona, M. & Gopalan, S. Isotope and temperature shifts of direct and indirect band gaps in diamond-type semiconductors. *Phys. Rev. B* **45**, 3376–3385 (1992).
31. Tan, P. H. *et al.* The shear mode of multilayer graphene. *Nat. Mater.* **11**, 294–300 (2012).
32. Molina-Sánchez, A. & Wirtz, L. Phonons in single-layer and few-layer MoS₂ and WS₂. *Phys. Rev. B* **84**, 155413 (2011).
33. Paszkowicz, W., Pelka, J. B., Knapp, M., Szyszko, T. & Podsiadlo, S. Lattice parameters and anisotropic thermal expansion of hexagonal boron nitride in the 10–297.5 K temperature range. *Appl. Phys. A* **75**, 431–435 (2002).
34. Yates, B., Overy, M. J. & Pirgon, O. The anisotropic thermal expansion of boron nitride. *Philos. Mag.* **32**, 847–857 (1975).
35. Popov, V. N. & Van Alsenoy, C. Low-frequency phonons of few-layer graphene within a tight-binding model. *Phys. Rev. B* **90**, 245429 (2014).
36. Gao, W. & Tkatchenko, A. Sliding mechanisms in multilayered hexagonal boron nitride and graphene: the effects of directionality, thickness, and sliding constraints. *Phys. Rev. Lett.* **114**, 096101 (2015).
37. Savini, G. *et al.* Bending modes, elastic constants and mechanical stability of graphitic systems. *Carbon* **49**, 62–69 (2011).
38. Serrano, J. *et al.* Vibrational properties of hexagonal boron nitride: inelastic X-ray scattering and ab initio calculations. *Phys. Rev. Lett.* **98**, 95503 (2007).
39. Vuong, T. Q. P. *et al.* Exciton-phonon interaction in the strong-coupling regime in hexagonal boron nitride. *Phys. Rev. B* **95**, 201202 (2017).
40. van Smaalen, S., Palatinus, L. & Schneider, M. The maximum-entropy method in superspace. *Acta Crystallogr. A* **59**, 459–469 (2003).
41. Yamamura, S., Takata, M. & Sakata, M. Charge density of hexagonal boron nitride using synchrotron radiation powder data by maximum entropy method. *J. Phys. Chem. Phys. Sol.* **58**, 177–183 (1997).
42. Topsakal, M., Aktürk, E. & Ciraci, S. First-principles study of two- and one-dimensional honeycomb structures of boron nitride. *Phys. Rev. B* **79**, 115442 (2009).
43. Catellani, A., Posternak, M., Baldereschi, A. & Freeman, A. J. Bulk and surface electronic structure of hexagonal boron nitride. *Phys. Rev. B* **36**, 6105–6111 (1987).
44. Yamanaka, T. & Morimoto, S. Isotope effect on anharmonic thermal atomic vibration and refinement of ¹²C and ¹³C diamond. *Acta Crystallogr. B* **52**, 232–238 (1996).
45. Nörtershäuser, W. & Geppert, C. in *The Euroschool on Exotic Beams* Vol. IV (eds Scheidenberger, C. & Pfützner, M.) 233 (Lecture notes in Physics 879, Springer, 2014).
46. Fleming, D. G., Manz, J., Sato, K. & Takayanagi, T. Fundamental change in the nature of chemical bonding by isotopic substitution. *Angew. Chem. Int. Ed.* **53**, 13706–13709 (2014).
47. Reilly, A. M. & Tkatchenko, A. Role of dispersion interactions in the polymorphism and entropic stabilization of the aspirin crystal. *Phys. Rev. Lett.* **113**, 055701 (2014).
48. Folpini, G. *et al.* Strong local-field enhancement of the nonlinear soft-mode response in a molecular crystal. *Phys. Rev. Lett.* **119**, 097404 (2017).
49. Watanabe, H., Nebel, C. E. & Shikata, S. Isotopic homojunction band engineering from diamond. *Science* **324**, 1425–1428 (2009).
50. Lovchinsky, I. *et al.* Magnetic resonance spectroscopy of an atomically thin material using a single-spin qubit. *Science* **355**, 503–507 (2017).

Acknowledgements

We gratefully acknowledge C. L'Henoret for his technical support at the mechanics workshop, and A. Dréau, V. Jacques and E. Rousseau for fruitful discussions. This work and the PhD funding of T.Q.P.V. were financially supported by the network GaNeX (ANR-11-LABX-0014). GaNeX belongs to the publicly funded *Investissements d'Avenir* program managed by the French ANR agency. G.C. is member of 'Institut Universitaire de France'. B.G. acknowledges the Russian Megagrant program (14.W03.31.0011) at the Ioffe Institute, Saint Petersburg, Russia. This work was also supported by the Spanish MINECO/FEDER under contract MAT2015-71305-R. The hBN crystal growth is based upon work supported by the National Science Foundation under Grant No. CMMI 1538127.

Author contributions

S.L. and J.H.E. synthesized the samples. T.Q.P.V., P.V. and G.C. performed photoluminescence spectroscopy. A.V.d.L. the X-ray diffraction measurements. R.C., L.A. and T.M. the Raman scattering experiments. All authors contributed to the interpretation of the results. The project was initiated by B.G. and the manuscript was written by G.C.

Additional information

Supplementary information is available in the online version of the paper. Reprints and permissions information is available online at www.nature.com/reprints. Publisher's note: Springer Nature remains neutral with regard to jurisdictional claims in published maps and institutional affiliations. Correspondence and requests for materials should be addressed to G.C.

Competing financial interests

The authors declare no competing financial interests.

Methods

Experiments. Experimental details are given in the Supplementary Methods, for the synthesis of the isotopically purified crystals, the measurements by photoluminescence or Raman scattering spectroscopy, and X-ray diffraction.

Data availability. X-ray diffraction data can be obtained from FIZ Karlsruhe, 76344 Eggenstein-Leopoldshafen, Germany (fax: (+49)7247-808-666; e-mail: crysdta@fiz-karlsruhe.de, on quoting the deposition numbers CSD-432896–432903). All other data on photoluminescence or Raman spectroscopy are available from the authors.